Research Article Vol. 17, No. 8 / 1 Aug 2026 / Biomedical Optics Express 4179
Biomedical Optics EXPRESS

Compact FPGA-based software correlator for real-time blood flow measurement with diffuse correlation spectroscopy

VINH-KHANH MAI,* VISHNUKUMAR RAGHU, PENAZ PARVEEN SULTANA MOHAMMAD, TRISTAN VALENZUELA, AND ASHWIN B. PARTHASARATHY

Dept. of Electrical and Computer Engineering, University of South Florida, 4202 E Fowler Avenue, Tampa, FL 33620, USA
khanhmai@usf.edu

Abstract: Diffuse correlation spectroscopy (DCS) enables noninvasive measurement of deep tissue blood flow, but high-speed and multi-channel implementations are often constrained by data throughput. We present an FPGA-based compressed DCS architecture for fast, high-throughput real-time measurements of intensity autocorrelation functions that leverages parity-based 1-bit photon counting to exploit sparse photon arrivals. The system is validated by direct comparison with a conventional research-grade DCS instrument with experiments on solid and liquid tissue-simulating phantoms and *in vivo* forearm measurements during arm-cuff occlusion. Results demonstrate 96.875% data compression with preservation of autocorrelation fidelity and blood flow estimation performance over practical acquisition rates, enabling compact and scalable real-time DCS instrumentation.

1. Introduction

Blood flow is a fundamental physiological parameter that reflects tissue metabolism, vascular function, and disease state. Noninvasive measurement of microvascular blood flow is therefore of broad interest across neuroscience, critical care, and vascular medicine. Among optical techniques, Diffuse Correlation Spectroscopy (DCS) [1–3] has become a widely used method for probing deep tissue blood flow by analyzing temporal fluctuations of multiply scattered coherent light, with applications spanning cerebral [4–6], muscular [7,8], and spinal cord [9] hemodynamics. Early implementations of DCS relied on dedicated hardware correlators [1,10,11], which provided robust measurements, but were limited in temporal resolution and flexibility. More recent work has demonstrated that software-based correlators can significantly improve acquisition speed and enable high temporal resolution measurements of blood flow dynamics, including pulsatile signals [12–15].

As a natural extension of these advances, a growing body of work has explored embedded and FPGA-based implementations to further improve system portability and enable real-time processing. Recent reviews by Wang *et al.* [16] and Carp *et al.* [17] make clear that current DCS hardware development is being driven by a common set of demands: higher signal-to-noise ratio (SNR), improved depth sensitivity, faster sampling for pulsatile and functional measurements, lower-cost, and more compact instrumentation. In particular, Carp *et al.* emphasize that conventional DCS faces a fundamental tradeoff between measurement noise performance and deep-tissue sensitivity, especially at larger source–detector separations where photon count rates fall and practical acquisition speeds become limited [17]. These constraints have motivated a broad shift toward hardware strategies that increase photon throughput and parallelize detection, including multi-source illumination and parallel single-speckle detection [18–20], heterodyne/interferometric detection [21], multispeckle camera-based methods [22–26],

#601793 https://doi.org/10.1364/BOE.601793
Journal © 2026 Received 15 Apr 2026; revised 13 Jun 2026; accepted 6 Jul 2026; published 17 Jul 2026

Biomedical Optics EXPRESS

long-pathlength photon selection [27–31], and longer-wavelength operation. [32–34]. While these approaches differ in implementation, they share a common architectural theme of extracting more usable flow information by sampling more photons, more speckles, or more depth-selective photon populations per unit time.

Wang *et al.* further show that this trend has been accompanied by rapid progress in detector and correlator technology, particularly through the adoption of highly integrated SPAD arrays and on-board digital processing [16]. Early multispeckle demonstrations used grouped discrete SPADs to realize the expected $\sqrt{N}$ gain in SNR from parallel speckle sampling, as shown by Dietsche *et al.* [18]. This direction was extended to integrated SPAD-array DCS platforms, beginning with a 5×5 system demonstrated by Johansson *et al.* [35] and subsequently scaling to 32×32 arrays [19,20], 192×128 arrays [36], and most recently 500×500 and 512×512 SPAD-camera systems for massively parallel, real-time multispeckle DCS [37,38]. At the correlator level, Wang *et al.* note that conventional hardware correlators remain attractive because they support high-speed real-time processing over wide lag-time ranges, but they are comparatively more expensive and less flexible than software-based alternatives [16]. This has motivated increasing interest in embedded correlators and FPGA implementations. Lin *et al.* [39] demonstrated real-time DCS analysis on an FPGA, and Moore and Lin [40] further showed on-board autocorrelation computation for embedded applications. Taken together, these studies indicate that the field is moving toward increasingly parallel and computation-rich DCS hardware. At the same time, they also underscore a central practical challenge: as detector count, sampling rate, and on-board processing demands increase, data movement and bandwidth become limiting system-level constraints rather than secondary implementation details.

Despite these advances, most existing FPGA-based and embedded DCS systems remain limited in channel count and sampling efficiency, typically supporting 4 measurement channels and/or sampling photon counts at ≈ 1 MHz. These limitations arise primarily from constraints in data throughput and hardware resource utilization. Conventional DCS architectures employ multi-bit photon counters and data representations that are optimized to work with general-purpose (typically) 32−bit counters/timers. These approaches do not account for the sparse photon arrival statistics characteristic of diffuse optics, and therefore incur significant bandwidth overhead, which restricts scalability to higher channel counts and faster sampling rates. To address these challenges, we recently introduced a compressed DCS framework based on reduced bit-depth photon encoding [41], demonstrating that sparse photon arrival statistics can be exploited to reduce data requirements without compromising the fidelity of estimated tissue blood flow. Here, we build on this concept, to realize a fully integrated architecture that combines compressed photon counting, high-speed acquisition, and scalable multi-channel processing within an embedded platform. Specifically, we present a compact FPGA-based DCS architecture that addresses both data throughput and scalability limitations by exploiting photon-arrival sparsity. The proposed system implements parity-based 1-bit photon counting, high-speed data streaming, and real-time fitting of blood flow indices without modifying the underlying DCS signal model. By reducing per-channel data width and bandwidth requirements, this approach enables high-rate, multi-channel DCS acquisition within the constraints of resource-limited embedded hardware.

We validate the system through direct, simultaneous comparison with a conventional research-grade DCS instrument using solid and liquid tissue-simulating phantoms and *in vivo* forearm measurements during an arm-cuff occlusion protocol. These experiments evaluate autocorrelation fidelity, blood flow estimation accuracy, signal-to-noise performance, and dynamic response under physiological conditions.

Biomedical Optics EXPRESS

2. System architecture and FPGA implementation

2.1. Overall system architecture

Diffuse correlation spectroscopy (DCS) measures deep tissue blood flow by quantifying temporal fluctuations in multiply scattered coherent light. In a typical DCS system, light from a long coherence length source is delivered to tissue, and light that has diffused and scattered through tissue is collected a short distance away using single-mode fibers. Motion of dynamic scatterers in the tissue, primarily red blood cells, causes decorrelation of the detected (speckle) intensity, which is quantified through the normalized intensity autocorrelation function $g_2(\tau)$. A blood flow index (BFI) is then estimated by fitting the measured autocorrelation function to a solution to the correlation diffusion model. We refer the reader to many excellent review articles that describe DCS theory and applications in greater detail [1,2,16]; here we focus on the instrumentation to convert detected light to DCS intensity autocorrelation functions.

Our DCS platform is organized around a hardware–software co-design in which time-critical photon detection and counting are executed on an embedded FPGA, while computation of the autocorrelation function and estimation of blood flow are handled on a host computer. This division allows deterministic high-speed acquisition to be maintained at the hardware level while preserving flexibility for real-time signal processing and model fitting in software.

The optical subsystem employs a long-coherence length wavelength-stabilized 785-nm laser source (iBeam Smart, Toptica Photonics, Pittsford, NY) to illuminate tissue through a multimode source fiber. Diffusely scattered light is collected using single-mode detection fibers positioned at source–detector separations of 10 mm and 25 mm, corresponding to sensitivity predominantly to superficial and deeper tissue volumes, respectively. Photon detection is performed using four single-photon counting avalanche photodiodes (SPADs) (SPCM-AQ4C, Excelitas), each generating transistor–transistor logic (TTL) pulses corresponding to individual photon arrival events, as shown in Fig. 1. TTL outputs from the SPADs are first conditioned and level-shifted using auxiliary interface hardware (NI myRIO-1900, National Instruments, Austin, TX) to ensure electrical compatibility with the FPGA digital inputs. The conditioned signals are then routed to an embedded FPGA platform (NI sbRIO-9607, National Instruments, Austin, TX), where photon counting, data packing, and streaming are implemented in real time. Processed data are transmitted continuously to the host computer over a Gigabit Ethernet link, enabling low-latency, sustained operation suitable for real-time monitoring.

For the purposes of this paper, each SPAD output is internally replicated on the interface hardware and routed to multiple independent photon counting blocks on the FPGA. This configuration allowed us to evaluate the performance of 16 parallel acquisition channels derived from four physical detectors. FPGA measurements were compared with a conventional DCS instrument with a LabVIEW-based software correlator, as described in our previous publications [12,42,43]. The TTL outputs from the SPADs were connected directly to the software correlator for simultaneous measurements of autocorrelation functions with both systems.

2.2. Photon arrival statistics and sparsity in DCS measurements

We first establish the sparsity of photon arrival statistics in DCS measurements, building on our prior work [41]. Photon detection in DCS follows a doubly-stochastic process. The photon counts recorded in each bin are Poisson-distributed, while the intensity itself fluctuates according to temporally correlated speckle statistics; these correlations appear between bins and do not alter the single-bin marginal distribution relevant here [44,45]. More precisely, the marginal count distribution in a bin approaches, and is well approximated as Poisson with a fixed $\lambda = R\Delta t$, in the limit of low per-bin photon occupancy ($\lambda << 1$), where R is the mean photon arrival rate and Δt is the bin duration/width. [44] Further, the probability of observing two or more photons in a single

Biomedical Optics EXPRESS

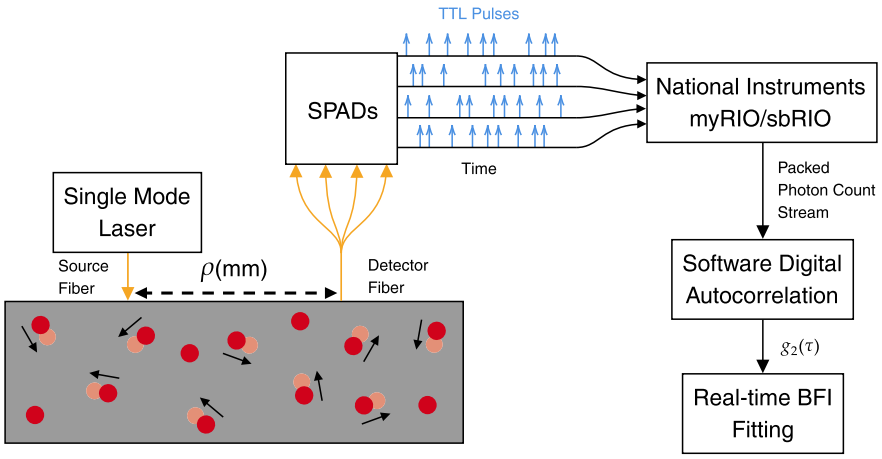

Fig. 1. Schematic of the DCS measurement configuration in a semi-infinite geometry. Coherent laser light is delivered to tissue via optical fibers, and diffusely scattered light is collected by single-mode detection fibers. Photon arrival events detected by single-photon counting avalanche photodiodes (SPADs) are converted to TTL pulses and routed to the FPGA-based acquisition system. The resulting intensity autocorrelation function $g_2(\tau)$ is fit to a correlation diffusion model to estimate blood flow index in real time.

bin is given by

$$P(n \geq 2) = 1 - e^{-\lambda}(1 + \lambda). \tag{1}$$

Under typical operating conditions, photon count rates per detector channel range from 20 to 500 kHz. In the system considered here, photon arrivals are sampled at 10 MHz, corresponding to a bin duration of 100 ns. For these representative operating conditions, Table 1 shows that the probability of detecting two or more photons per bin is very small.

Table 1. Sparsity of photon counts in typical DCS measurements. Column 3 shows the probability of detecting 2 or more photons in 100 ns detection bin at different photon count rates

R	$\lambda = R\Delta t$	$P(n \geq 2)$
20 kHz	0.002	0.0002%
50 kHz	0.005	0.001%
200 kHz	0.02	0.02%
500 kHz	0.05	0.12%

Thus, under typical DCS operating conditions, the vast majority of time bins contain either zero or one detected photon. This sparsity implies that the information relevant for estimating the intensity autocorrelation function is dominated by binary occupancy of time bins rather than precise multi-photon count values. This observation motivates the use of parity-based 1-bit photon counting in the present work.

2.3. FPGA-based photon counting and data streaming

Figure 2 shows a schematic representation of the FPGA-based photon counting for DCS. Photon arrival events at each acquisition channel are recorded using 1-bit photon counters implemented directly on the FPGA (using LabVIEW). Rather than accumulating multi-bit photon counts over

Biomedical Optics EXPRESS

each sampling interval, each counter records the parity of photon arrivals within a fixed time bin, such that the counter output toggles on each detected photon event. As a result, the recorded value reflects whether an odd or even number of photons arrived during the bin interval. While multiple photon arrivals within a single time bin may result in counter overflow, the probability of such events is negligible for the photon count rates and bin durations used in this work, and their contribution is statistically indistinguishable from shot noise in the autocorrelation analysis.

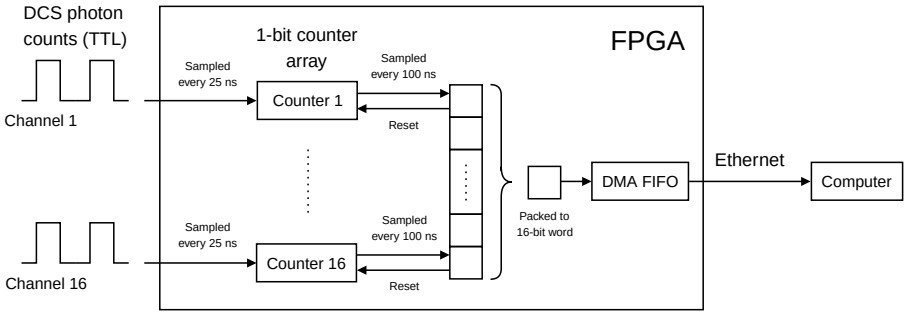

Fig. 2. Block diagram of the FPGA-based photon counting and data streaming architecture. TTL outputs from individual SPADs are routed to digital input/output (DIO) pins on the FPGA, where parity-based 1-bit counters register photon arrivals. The outputs from 16 parallel counters are packed into a 16-bit word at each sampling instant and written to a Direct Memory Access First-In First-Out (DMA FIFO) buffer for transfer via Gigabit Ethernet to the host computer. The FPGA resets all 1-bit counters at a sampling frequency of f_S = 10 MHz. For an integration time of t_{int} = 50 ms, 500,000 samples per channel are acquired.

The FPGA operates with a 40 MHz internal clock, while photon sampling is performed at an effective rate of 10 MHz, corresponding to a bin width of 100 ns. At the end of each sampling interval, all counters are synchronously reset, ensuring that photon arrivals are registered only within the defined bin duration. This timing strategy preserves sensitivity to short correlation delays while enabling deterministic, high-throughput data acquisition.

In contrast to conventional photon counting architectures that allocate 32 bits per channel to store photon counts [12], the present design uses a single bit per channel. Under sparse photon arrival conditions, this representation retains the statistically dominant information required for autocorrelation estimation while dramatically reducing hardware resource usage and data bandwidth. Data from all 16 channels are sampled synchronously and packed into a single 16-bit word at each sampling instant, with one bit corresponding to each channel. This compact data format enforces strict temporal alignment across channels and simplifies downstream parsing and processing. All counting and packing operations are performed fully in parallel on the FPGA, avoiding time-multiplexing and ensuring uniform latency across channels. The packed photon arrival stream is transmitted continuously from the FPGA to the host computer over Gigabit Ethernet at a sustained data rate of approximately 160 Mbps. For comparison, an equivalent system employing 32-bit counters at the same sampling rate and channel count would require data throughput of about 5.12 Gbps, exceeding the practical limits of standard embedded communication interfaces. Our parity-based 1-bit counting architecture realizes a 96.875% lossless data compression efficiency, and therefore enables high-speed, multi-channel DCS acquisition within the constraints of compact embedded hardware.

The streaming framework supports uninterrupted real-time operation, with stable data transfer observed during extended acquisition periods. This architecture enables continuous DCS measurements without buffering-induced delays, facilitating real-time physiological monitoring and dynamic experimental protocols.

Biomedical Optics EXPRESS

2.4. DCS autocorrelation function and blood flow index processing

Computation of DCS intensity autocorrelation functions is performed on the host computer using custom software developed in LabVIEW (National Instruments, Austin, TX). Real-time processing and fitting of autocorrelation functions were performed on a laptop equipped with a 13^{th} Gen Intel Core i9-13900HX processor (24 cores, 32 logical processors) and 31.7 GB RAM, running Microsoft Windows 11 Home (64-bit). The real-time acquisition/analysis software was implemented in LabVIEW 2019 32-bit. No GPU acceleration was used; autocorrelation processing and BFI fitting were performed on the host CPU. During the *in vivo* experiments, this host-computer configuration sustained 20 Hz real-time BFI updates without dropped frames. The normalized intensity autocorrelation function is computed from the streamed photon arrival data according to

$$g_2(\tau = \Delta n \Delta t) = \frac{\langle n(i)\, n(i+\Delta n)\rangle}{\langle n(i)\rangle^2}, \tag{2}$$

where $n(i) \in \{0, 1\}$ denotes the parity-encoded photon arrival in the i-th time bin and Δn is the discrete delay index. For each acquisition channel, autocorrelation functions are computed at 90 logarithmically spaced delay times spanning from 100 ns to 88.8 μs using a single-tau architecture [12]. This delay range was selected to capture the full decorrelation observed in the phantom and *in vivo* measurements reported here.

Estimation of DCS blood flow index (BFI) is performed by fitting the measured $g_2(\tau)$ curves to a semi-infinite homogeneous solution of the correlation diffusion equation [1,11]. In this framework, BFI corresponds to the parameter αD_B, where D_B is an effective Brownian diffusion coefficient and α is the fraction of dynamically scattering particles. The measured intensity autocorrelation function ($g_2(\tau)$) is related to the normalized electric field autocorrelation function ($g_1(\tau)$) through the Siegert relation,

$$g_2(\tau) = 1 + \beta |g_1(\tau)|^2, \tag{3}$$

where β is the speckle averaging factor.

The normalized electric field autocorrelation function $g_1(\tau)$ in turn is expressed as

$$g_1(\tau) = \frac{G_1(\rho, \tau)}{G_1(\rho, 0)}, \tag{4}$$

where $G_1(\rho, \tau)$ is the un-normalized electric field temporal correlation function at source–detector separation ρ. The semi-infinite homogeneous solution of the correlation diffusion equation describes $G_1(\rho, \tau)$ as,

$$G_1(\rho, \tau) = \frac{3}{4\pi l_{tr}} \left[\frac{\exp(-K(\tau) r_1)}{r_1} - \frac{\exp(-K(\tau) r_b)}{r_b} \right], \tag{5}$$

where $l_{tr} = 1/(\mu_a + \mu_s')$ is the transport mean free path, $r_1 = \sqrt{l_{tr}^2 + \rho^2}$, $r_b = \sqrt{(l_{tr} + 2z_b)^2 + \rho^2}$, ρ is the source–detector separation, μ_a is the tissue absorption coefficient, μ_s' is the tissue reduced scattering coefficient, $z_b = \left[2 l_{tr}(1 + R_{eff})\right] / \left[3(1 - R_{eff})\right]$, and R_{eff} is the Fresnel effective reflection coefficient. The dynamic wave-vector $K(\tau)$ depends on BFI according to

$$K(\tau) = \sqrt{3\mu_a\,(\mu_a + \mu_s') \left(1 + 2k_0^2 \alpha D_B \tau \frac{\mu_s'}{\mu_a}\right)}, \tag{6}$$

where $k_0 = 2\pi n/\lambda$ is the optical wavenumber in tissue, n is the refractive index, and λ is the laser wavelength.

Biomedical Optics EXPRESS

For each acquisition frame, the measured $g_2(\tau)$ curve was fit to the analytical solution using a Nelder–Mead nonlinear optimization algorithm. The absorption coefficient μ_a and reduced scattering coefficient μ_s' were assumed from literature values appropriate for the measurement wavelength and sample type, while the fitting estimated BFI and β. Fixed initial guesses and bounded parameter ranges were applied to ensure numerical stability, and the full delay range was included in the fitting procedure.

Real-time fitting was enabled for the *in vivo* experiments, where BFI estimates were updated at each integration interval (t_{int} = 50 ms) during data acquisition. The real-time fitting routine uses the measured $g_2(\tau)$ curves and the semi-infinite homogeneous tissue model described above. The required inputs to the fitting routine include source–detector separation, the assumed absorption coefficient μ_a and reduced scattering coefficient μ_s', refractive indices of the tissue and surrounding medium, and the laser wavelength. The present implementation demonstrates real-time operation at 20 Hz using a high-performance host laptop; lower-power computers may require optimization of the fitting routine, reduced model complexity, or longer integration times depending on the desired update rate. For phantom experiments, the same fitting framework was applied offline in MATLAB (MathWorks, Natick, MA) to ensure direct comparison between the FPGA-based and conventional systems without altering the acquisition workflow. For the *in vivo* experiments, three analysis streams are reported. "FPGA post-processed" refers to BFI estimated in MATLAB from $g_2(\tau)$ curves acquired in real time with the FPGA-DCS system. "DCS reference post-processed" refers to BFI estimated in MATLAB from $g_2(\tau)$ curves acquired in real time with the conventional DCS reference system. "FPGA real-time" refers to BFI estimated in LabVIEW from $g_2(\tau)$ curves acquired in real time by the FPGA-DCS system, with BFI fitting performed in software on the host laptop. Thus, the proposed method is the FPGA-DCS acquisition system, and the post-processed and real-time traces demonstrate offline validation and online operation of the same FPGA-based acquisition architecture.

3. Experiments and results

3.1. Validation approach

Experimental validation was structured as a direct comparison between the FPGA-based DCS system and a conventional research-grade implementation. To isolate the effects of the photon counting and correlator architecture, both systems were operated concurrently using identical photon arrival streams. TTL pulses from the SPAD detectors were split and routed simultaneously to the FPGA-based acquisition system and to a conventional 32-bit counter-based software correlator. Agreement between the two systems was evaluated using controlled phantom experiments and *in vivo* measurements.

3.2. Solid phantom validation

The first validation experiment examined the ability of the FPGA-based DCS system to accurately acquire intensity autocorrelation functions under static scattering conditions. Measurements were performed on a solid tissue-simulating phantom with optical properties of μ_a = 0.156 cm^{-1} and μ_s' = 4.8 cm^{-1} at 785 nm (ISS Inc., Champaign, IL). The DCS probe was secured to the phantom surface, and measurements were obtained at source–detector separations of 10 mm and 25 mm.

Photon arrival data were acquired using the FPGA-based correlator with a sampling frequency of $f_{sampling}$ = 10 MHz and an integration time of t_{int} = 50 ms, corresponding to an effective acquisition rate of 20 Hz. Each acquisition frame consisted of a 500,000-point sequence of 1-bit photon data per channel. Intensity autocorrelation functions were computed using 90 digital delays ranging from 1 to 888 samples, corresponding to correlation delay times from 100 ns to 88.8 μs.

Biomedical Optics EXPRESS

Figure 3 shows representative $g_2(\tau)$ curves obtained from the solid phantom at both source–detector separations using the FPGA-based system and the conventional DCS reference system. As expected for a static scattering medium, the measured autocorrelation functions exhibit no decay over the examined delay range. The close agreement between the FPGA-based and reference measurements confirms that the FPGA-based architecture accurately preserves autocorrelation structure in the absence of dynamic scatterer motion, providing a baseline validation of system timing, photon counting, and correlation computation.

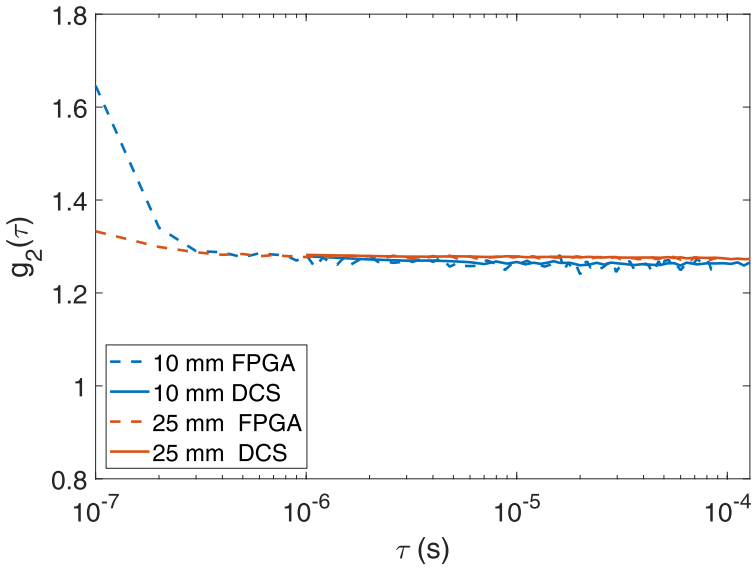

Fig. 3. Normalized intensity autocorrelation functions $g_2(\tau)$ measured from a solid tissue-simulating phantom using the FPGA-based DCS system (dashed lines) and a conventional DCS reference system (solid lines). Measurements were obtained at source–detector separations of 10 mm (blue) and 25 mm (red). The phantom optical properties were $\mu_a = 0.156$ cm^{-1} and $\mu_s' = 4.8$ cm^{-1} at 785 nm. Curves represent averages over 1 minute of acquisition with an integration time of 50 ms.

3.3. *Liquid phantom validation*

Quantitative validation of blood flow estimation was next performed using a dynamic, tissue-simulating liquid phantom. The purpose of this experiment was to assess whether the FPGA-based DCS system preserves both the shape of the intensity autocorrelation function and the accuracy of derived blood flow indices under controlled dynamic scattering conditions.

The liquid phantom was prepared from Intralipid (20% emulsion, Sigma-Aldrich, MO), India ink, and distilled water to achieve optical properties of $\mu_a = 0.05$ cm^{-1} and $\mu_s' = 10$ cm^{-1} at 785 nm. The DCS probe was positioned on the phantom surface, and intensity autocorrelation functions were acquired simultaneously using the FPGA-based DCS system and a conventional DCS reference system at an acquisition rate of 20 Hz. Measurements were obtained at source–detector separations of 10 mm and 25 mm. Detector photon count rates during these measurements were maintained at approximately 60 kHz at both source–detector separations.

Figure 4 shows representative normalized intensity autocorrelation functions $g_2(\tau)$ measured with the FPGA-based system at both separations. Each curve represents an average over 1 minute of acquisition, with individual autocorrelation functions computed using an integration time of 50 ms. The observed decay of $g_2(\tau)$ arises from dynamic scattering due to Brownian motion of

Biomedical Optics EXPRESS

lipid particles in the Intralipid solution. Faster decorrelation is observed at the 25-mm separation relative to the 10-mm separation, consistent with the increased photon pathlength and enhanced sensitivity to dynamic scattering at larger source–detector distances. Autocorrelation functions measured with the FPGA-based system closely match those obtained with the conventional DCS reference, exhibiting comparable decay profiles across the full delay range.

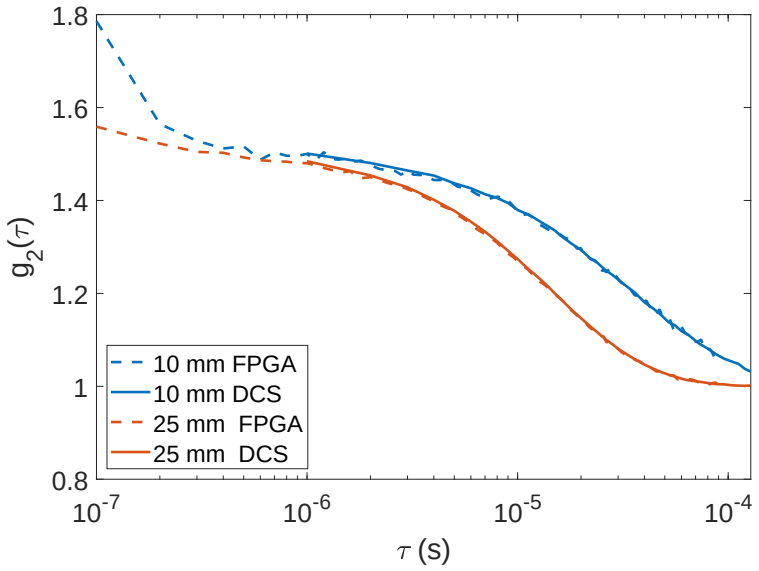

Fig. 4. Normalized intensity autocorrelation functions ($g_2(\tau)$) measured from a tissue-simulating liquid phantom using the FPGA-based DCS system (dashed lines) and a conventional DCS reference system (solid lines). Measurements were obtained at source–detector separations of 10 mm (blue) and 25 mm (red). The liquid phantom optical properties were $\mu_a = 0.05$ cm^{-1} and $\mu_s' = 10$ cm^{-1} at 785 nm. Curves represent averages over 1 minute of acquisition with an integration time of 50 ms.

To quantitatively compare blood flow estimates, intensity autocorrelation functions from both systems were fit to the semi-infinite correlation diffusion model to extract blood flow indices (BFI). Figure 5 summarizes this comparison for both source–detector separations. Scatter plots in Figs. 5(A) and 5(C) show BFI values estimated simultaneously by the FPGA-based and conventional systems at 10-mm and 25-mm separations, respectively. Corresponding time traces of BFI are shown in Figs. 5(B) and 5(D). The scatter plots in Figs. 5(A) and 5(C) show the BFI distributions over the full approximately 1-minute acquisition window, whereas the time traces in Figs. 5(B) and 5(D) show representative 20-second segments from 20 s to 40 s. Therefore, BFI values that appear in the full-distribution scatter plots may not appear within the shorter representative time traces. At a source–detector separation of 10 mm, the FPGA-based DCS system estimated a mean blood flow index of $(1.00 \pm 0.42) \times 10^{-8}$ cm^2/s, while the conventional DCS system estimated $(0.865 \pm 0.134) \times 10^{-8}$ cm^2/s. At 25 mm, the FPGA-based system estimated $(0.549 \pm 0.177) \times 10^{-8}$ cm^2/s, compared to $(0.492 \pm 0.128) \times 10^{-8}$ cm^2/s measured with the conventional system. Values are reported as mean ± standard deviation over the 1-minute acquisition window. Across both separations, the FPGA-based and conventional measurements exhibit comparable central values and variability. BFI values measured with FPGA-DCS are slightly higher than those measured with conventional DCS. This may be due to small differences in the measured autocorrelation functions. We further explore bias in our measurements with correlation and Bland–Altman analyses of the measured $g_2(\tau)$.

Biomedical Optics EXPRESS

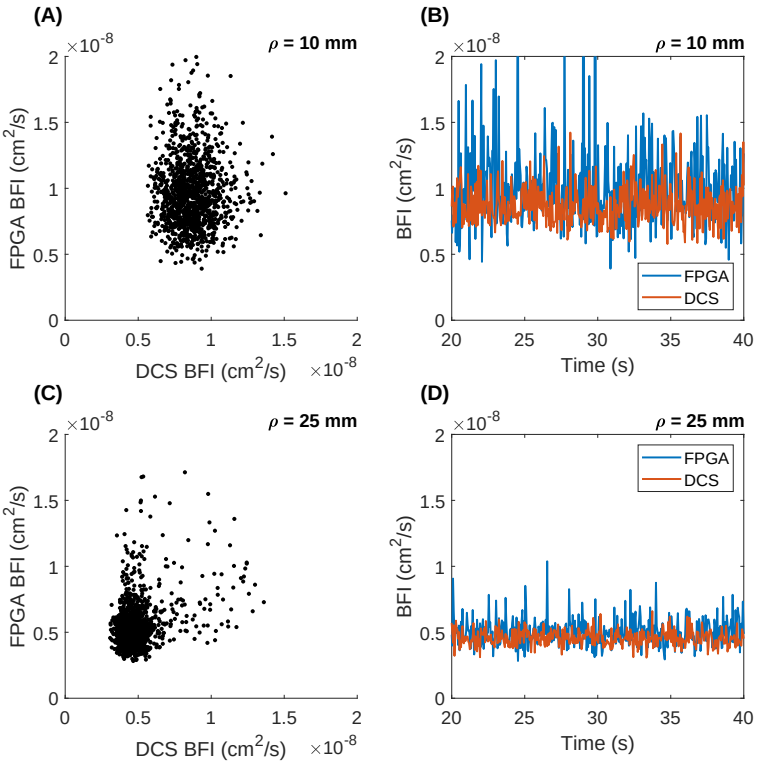

Fig. 5. Comparison of blood flow indices (BFI) estimated from a tissue-simulating liquid phantom using the FPGA-based DCS system and a conventional DCS reference system. (A) and (C) show scatter plots of simultaneously measured BFI values over the full 1-minute acquisition window at source–detector separations of 10 mm and 25 mm, respectively. (B) and (D) show corresponding time courses of BFI estimated by the FPGA-based system (blue) and the conventional system (red) for a representative 20-second segment from 20 s to 40 s.

3.4. *Noise, signal-to-noise ratio, and operating limits*

The signal-to-noise characteristics of the FPGA-based DCS system were further evaluated using the liquid phantom. Noise in the measured intensity autocorrelation function, $\sigma(\tau)$, was defined as the standard deviation of the measured autocorrelation function $g_2(\tau)$, and the corresponding signal-to-noise ratio (SNR) was defined as $\zeta(\tau) = (g_2(\tau) - 1)/\sigma(\tau)$ [46]. Autocorrelation functions were recorded at a source–detector separation of 25 mm while systematically varying both photon count rate and integration time. Photon count rates of 20 kHz, 50 kHz, and 400 kHz were achieved by adjusting the incident optical power, and integration times were varied from 1 ms to 100 ms.

Representative reductions in variability of $g_2(\tau)$ with increasing integration time are shown in Fig. 6 for delay times of 0.8 μs, 5.2 μs, and 20 μs. Corresponding noise and SNR measurements are summarized in Fig. 7. Here, the measured noise and SNR were fit to the DCS correlation noise model [46]. Across all examined delay times, measurement noise decreases and SNR increases with increasing integration time and photon count rate, consistent with established DCS noise models. The measured noise and SNR trends are well described by model fits over the explored parameter range, consistent with prior implementations of compressed sensing for DCS [41] and conventional DCS software correlators [12,43].

Biomedical Optics EXPRESS

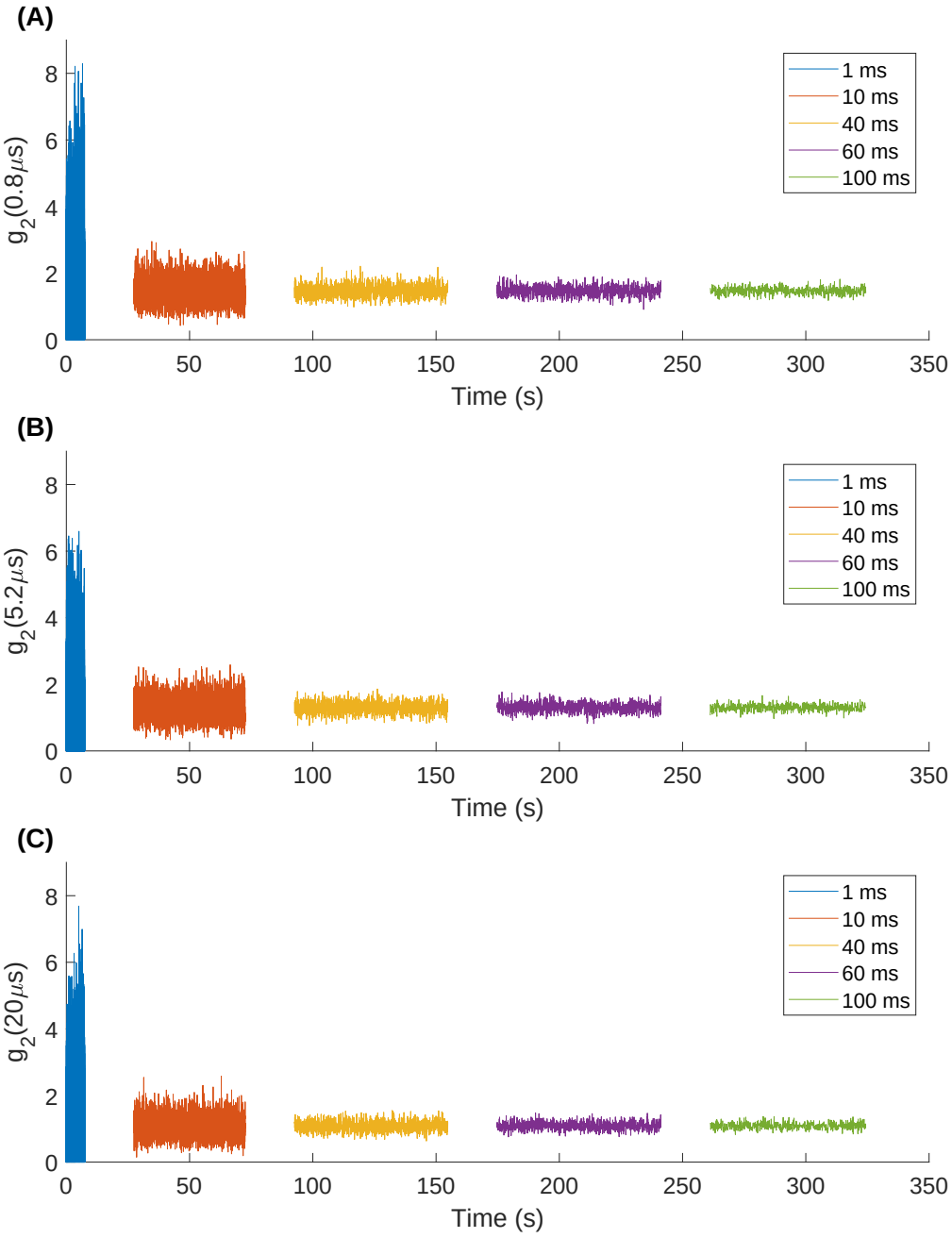

Fig. 6. Representative temporal fluctuations of the measured intensity autocorrelation function $g_2(\tau)$ at delay times of (A) 0.8 μs, (B) 5.2 μs, and (C) 20 μs for integration times of 1 ms, 10 ms, 40 ms, 60 ms, and 100 ms. Data were acquired from a tissue-simulating liquid phantom using the FPGA-based DCS system.

Biomedical Optics EXPRESS

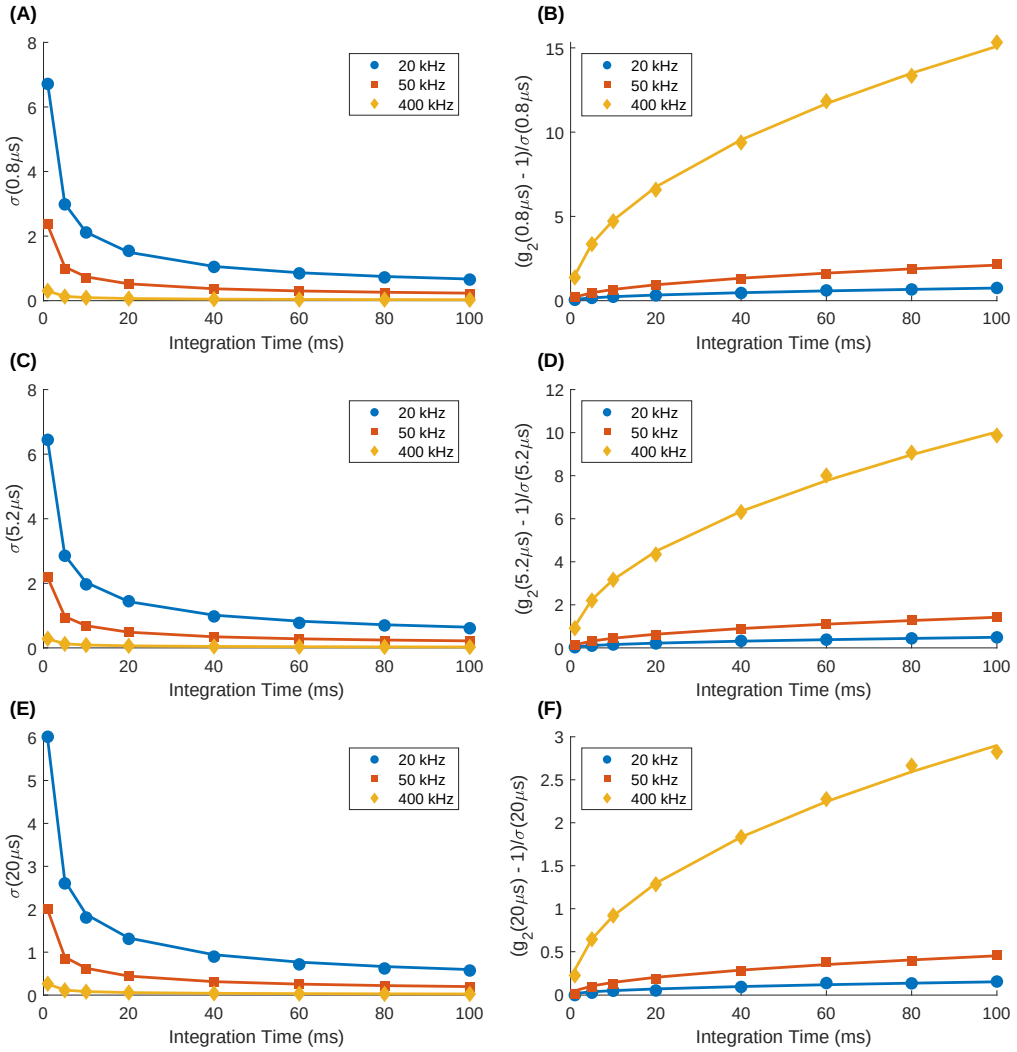

Fig. 7. Noise and signal-to-noise ratio (SNR) of intensity autocorrelation measurements obtained with the FPGA-based DCS system from a tissue-simulating liquid phantom. (A), (C), and (E) show the standard deviation $\sigma(\tau)$ of $g_2(\tau)$ at delay times of 0.8 μs, 5.2 μs, and 20 μs, respectively. (B), (D), and (F) show the corresponding SNR values. Measurements were performed at photon count rates of 20 kHz (blue), 50 kHz (red), and 400 kHz (yellow). Solid lines represent fits to a DCS correlation noise model.

At higher photon count rates, however, deviations between the FPGA-based and conventional systems become apparent, reflecting a breakdown of the photon sparsity condition inherent to 1-bit photon counting. To examine this effect quantitatively, $g_2(\tau)$ values measured by the FPGA-based system were compared with those measured by the conventional DCS reference system across integration times from 1 ms to 100 ms at photon count rates of 20 kHz, 50 kHz, and 400 kHz. Figure 8 summarizes this comparison using representative $g_2(\tau)$ curves, correlation scatter plots, and Bland–Altman analyses. In the Bland–Altman analysis, the mean bias was calculated as the mean paired difference between $g_2(\tau)$ measured by the FPGA-based system and $g_2(\tau)$ measured by the conventional DCS reference. The standard deviation describes the

Biomedical Optics EXPRESS

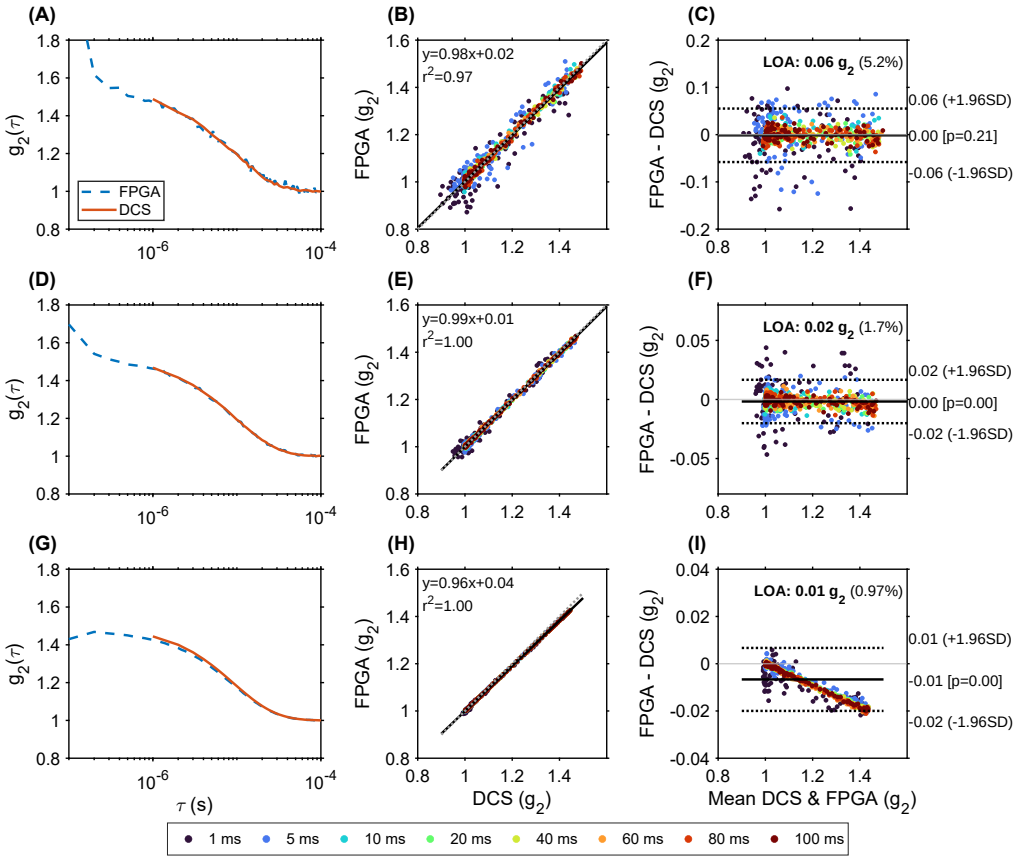

Fig. 8. Comparison of $g_2(\tau)$ measurements obtained from a tissue-simulating liquid phantom using the FPGA-based DCS system and a conventional DCS reference system. (A), (D), and (G) show representative normalized intensity autocorrelation functions, $g_2(\tau)$, measured at photon count rates of 20 kHz, 50 kHz, and 400 kHz, respectively, with an integration time of 40 ms. (B), (E), and (H) show the corresponding correlation scatter plots comparing FPGA-based and conventional $g_2(\tau)$ values across integration times from 1 ms to 100 ms. (C), (F), and (I) show the corresponding Bland–Altman analyses, where the difference is defined as FPGA minus conventional DCS. Measurements were obtained at a source–detector separation of 25 mm. Agreement between the two systems is strongest at 20 kHz and 50 kHz, while systematic underestimation by the FPGA-based system is observed at 400 kHz, particularly at short correlation delay times.

spread of these paired differences, and the limits of agreement were calculated as the mean bias ± 1.96 standard deviations. Thus, a mean bias near zero and narrow limits of agreement indicate close agreement between the two measurement systems. At lower photon count rates, strong agreement is observed across delay times and integration windows. At the highest photon count rate of 400 kHz, systematic underestimation of $g_2(\tau)$ by the FPGA-based system is observed, particularly at short delay times corresponding to larger $g_2(\tau)$ values. This behavior is consistent with increased multi-photon occupancy within individual time bins and highlights the practical operating regime in which the assumption of sparse photon statistics remains valid.

Biomedical Optics EXPRESS

3.5. In vivo validation

In vivo experiments were performed to evaluate the performance of the FPGA-based DCS system under physiologically relevant conditions and to assess its ability to capture both rapid and large-amplitude changes in blood flow. Validation was carried out on the forearm of a healthy adult volunteer using a transient arm-cuff occlusion protocol, with simultaneous measurements acquired using the FPGA-based system and a conventional DCS reference. Figure 9 shows a schematic of the experiment.

An optical probe, described previously, was secured on the forearm and connected to the illumination source and single-photon counting detectors via optical fibers. Outputs from the detectors were split and routed concurrently to the FPGA-based acquisition system and to a conventional DCS software correlator, ensuring that both systems processed identical photon arrival streams. Data acquisition and control for both systems were implemented using custom LabVIEW software. A pneumatic arm cuff was placed on the upper arm near the probe and connected to an automated inflation system (ATS4000, Zimmer Biomet, CA). The experimental protocol consisted of three sequential phases: a 1-minute baseline period, a 1-minute occlusion phase with cuff inflation to 160 mmHg, and a 1-minute post-occlusion recovery period. Intensity autocorrelation functions were recorded continuously at an acquisition rate of 20 Hz, and blood flow indices were computed as described earlier. All procedures were approved by the Institutional Review Board of the University of South Florida, and written informed consent was obtained from the participant prior to the experiment.

Baseline measurements acquired at a source–detector separation of 25 mm exhibit temporal fluctuations in the estimated blood flow index that are consistent with cardiac pulsatility. A representative baseline time course measured using the FPGA-based system is shown in Fig. 10(A). Periodic oscillations corresponding to the cardiac cycle are evident, and finer waveform features are preserved in the signal. The corresponding frequency spectrum, shown in Fig. 10(B), contains a dominant peak near the subject's heart rate along with higher-order harmonics, indicating that the FPGA-based architecture preserves sensitivity to fast physiological variations in blood flow.

The response of the system to a large, transient perturbation in blood flow was evaluated during arm-cuff occlusion. Figure 11 shows the time courses of blood flow indices estimated by the FPGA-based system and the conventional DCS reference throughout the baseline, occlusion, and recovery phases. During cuff inflation, both systems record a pronounced reduction in blood flow at the measurement site, followed by a rapid increase upon cuff release. The magnitude, timing, and overall shape of the measured flow changes are consistent across systems, demonstrating that the FPGA-based implementation accurately tracks both abrupt decreases and subsequent reperfusion over a wide dynamic range.

Importantly, the FPGA-based system captures these dynamics both in real time and in post-processed analysis without observable degradation in temporal resolution or signal stability relative to the conventional reference. The agreement between systems across baseline pulsatility and occlusion-induced flow changes confirms that the FPGA-based correlator and photon counting architecture preserve the essential features of the DCS signal under *in vivo* conditions.

4. Discussion

This work presents an FPGA-based DCS architecture designed to support high-rate photon sampling and real-time computation of intensity autocorrelation functions under the constraints of compact, resource-limited hardware. Rather than modifying the underlying DCS signal model, the proposed system targets inefficiencies in conventional photon counting and data handling, enabling substantial reductions (96.875%) in data bandwidth and throughput requirements while preserving compatibility with established analysis frameworks. This compression efficiency is higher than our prior work [41] and enables real-time, multi-channel measurement of DCS

Biomedical Optics EXPRESS

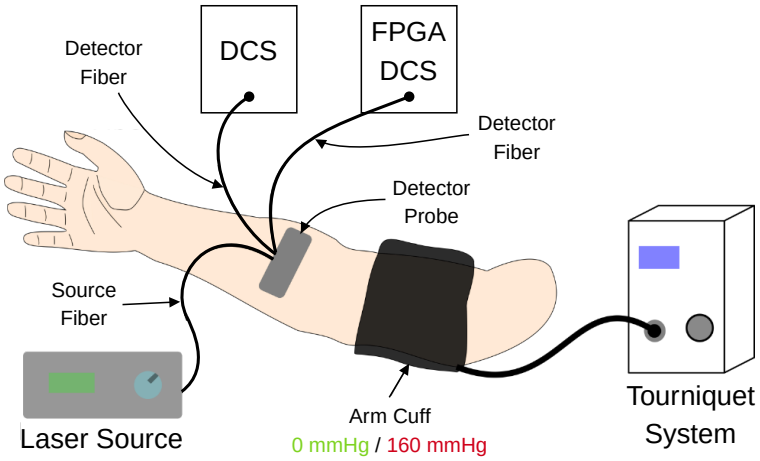

Fig. 9. Experimental configuration for *in vivo* arm-cuff occlusion measurements. An optical probe was positioned on the forearm, and detector outputs were split and routed simultaneously to the FPGA-based DCS acquisition system and a conventional DCS reference system. An arm cuff placed on the upper arm was inflated to 160 mmHg to induce transient vascular occlusion.

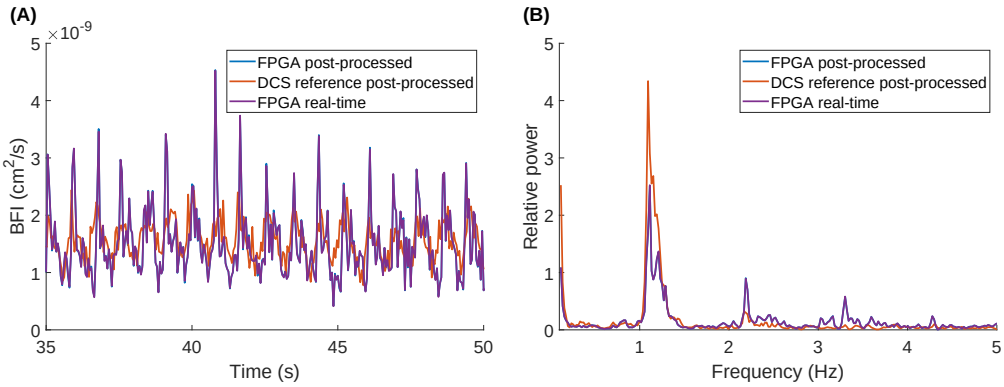

Fig. 10. Baseline blood flow dynamics measured on a human forearm using the FPGA-based DCS system at a source–detector separation of 25 mm. (A) Time course of the estimated blood flow index during the baseline period. (B) Frequency spectrum of the baseline blood flow trace, showing a dominant component near the subject's heart rate and corresponding harmonics. Results are shown for FPGA post-processed measurements, DCS reference post-processed measurements, and FPGA real-time measurements.

autocorrelation functions. We note that Wang *et al.* have implemented a similar correlator under photon-starved conditions [47,48].

In the present implementation, the FPGA is used for the timing-critical and bandwidth-limiting portions of the measurement, including photon detection, parity-based 1-bit counting, channel packing, and deterministic data streaming, while autocorrelation and model fitting are performed in software on the host computer. This hardware–software division reduces FPGA resource requirements and preserves flexibility in the correlation and fitting workflow. In particular, the lag-time structure, fitting routine, and physiological model assumptions can be modified in software without re-synthesizing the FPGA design. This is useful for direct comparison

Biomedical Optics EXPRESS

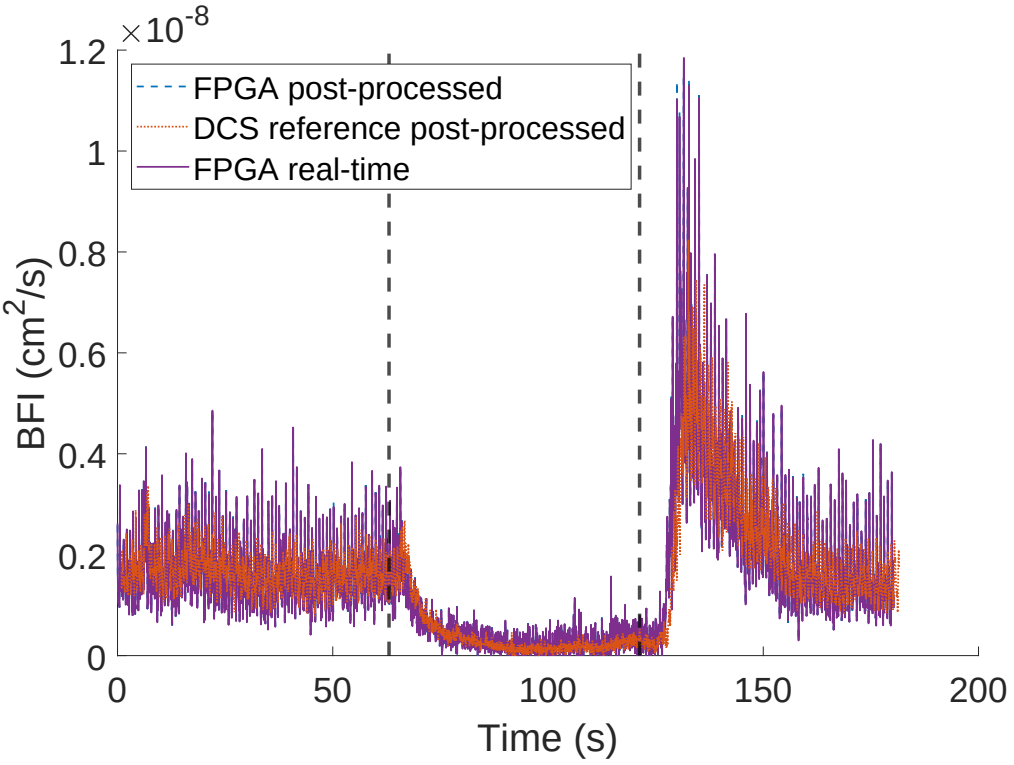

Fig. 11. Blood flow index time courses measured during arm-cuff occlusion and recovery at a source–detector separation of 25 mm. Results are shown for FPGA post-processed measurements (blue dashed), DCS reference post-processed measurements (red dotted), and FPGA real-time measurements (magenta solid). Vertical black lines mark the occlusion period.

with conventional DCS systems and for implementing both post-processed and real-time BFI estimation workflows. Fully embedded FPGA or on-chip autocorrelators provide an attractive alternative for highly integrated standalone systems and very large detector arrays, but they require additional on-chip logic resources and offer less flexibility for changing analysis algorithms. For example, recent DCS analysis algorithms account for heterogeneous (two- or three-layer) tissue geometries [49,50]. Our approach allows flexibility for retrospective analysis of DCS data with improving analytical diffusion models. Thus, the present architecture can be viewed as a complementary approach that uses the FPGA to reduce photon data bandwidth at the acquisition stage while preserving software flexibility for real-time DCS analysis.

Prior implementations of FPGA-based correlators have been effective for low channel counts (up to 8) and 1μs sampling times [39,51,52]. Recent implementations have focused on using FPGAs for SPAD arrays [20,36,40], also with 1μs sampling times. Computing autocorrelation decays with 100 ns sampling allows accurate computation of the early-lag portion of the autocorrelation function, which often allows better characterization of β and after-pulsing effects in 1064 nm DCS systems. Furthermore, in pathlength-resolved DCS systems, the autocorrelation decay of long photon pathlengths can occur at sub-microsecond timescales [29,53–55], which are better captured with 100 ns sampling of photon counts.

Experimental results across static and dynamic scattering conditions demonstrate that the FPGA-based implementation faithfully reproduces the autocorrelation structure comparable

Biomedical Optics EXPRESS

with a conventional research-grade DCS system. FPGA-based measurements of the intensity autocorrelation function deviate from ideal behavior at very short delay times. The upward deviation is a known artifact caused by afterpulsing in the SPADs [21]. Measurements on solid and liquid tissue-simulating phantoms confirm accurate timing, correlation computation, and flow estimation over a range of source–detector separations. Systematic characterization of measurement noise shows that the signal-to-noise behavior of the FPGA-based system follows established DCS noise models across practical integration times and photon count rates. *In vivo* measurements further demonstrate that the FPGA-based architecture captures both fast physiological fluctuations and large-amplitude flow changes. Baseline recordings preserve cardiac-related oscillations in blood flow, while arm-cuff occlusion experiments show that the system accurately tracks pronounced flow reductions and subsequent reperfusion. Agreement between FPGA-based and conventional measurements across these conditions indicates that the FPGA design maintains temporal resolution and dynamic range comparable to standard DCS instrumentation.

Taken together, these results establish that an FPGA-based correlator architecture can support real-time DCS measurements without compromising accuracy, sensitivity, or interpretability of the signal. By decoupling high-speed photon acquisition from bandwidth-intensive data representations, this approach provides a practical pathway toward scalable, embedded DCS systems suitable for continuous physiological monitoring and future multi-channel implementations. Notably, the parity-based 1-bit architecture required only modest FPGA resource usage in the sbRIO-9607, using 3641 of 13,300 slices (27.4%), 9,227 of 53,200 LUTs (17.3%), and 6 of 140 block RAMs (4.3%), while requiring no DSP48 resources and meeting timing requirements at 40 MHz. These results indicate that the design is not memory intensive and is well suited for hardware-software co-design on resource-constrained FPGA platforms. Furthermore, the 1-bit photon counting strategy may be adaptable to other photon-starved correlation-based applications, such as fluorescence correlation spectroscopy, provided that photon sparsity requirements are satisfied and the reduced bit-depth representation preserves the relevant signal information.

Finally, we note that deviations from photon sparsity can significantly affect the measured autocorrelation functions and blood flow indices. At photon count rates of $\approx$ 500 kHz, the probability of detecting 2 or more photons is very low (0.12%); however, violations of the sparsity assumptions have an outsized effect. At elevated count rates, FPGA-measured autocorrelation values show a clear bias, which could affect the estimates of blood flow. Nevertheless, the 500 kHz threshold is high for most *in vivo* DCS implementations and therefore our FPGA-DCS system should have broad applicability.

5. Conclusion

We present a highly compressed FPGA-based diffuse correlation spectroscopy (DCS) system for high-rate photon sampling and real-time computation of intensity autocorrelation functions using resource-efficient hardware. We validated our system against conventional DCS software correlators in tissue-simulating phantoms and *in vivo* experiments. We highlighted the potential of the compressed sensing approach for multi-channel DCS systems with faster photon sampling, embedded processing and continuous physiological monitoring.

Funding. National Institutes of Health (R01NS135077); U.S. National Science Foundation (2239675).

Acknowledgment. We thank Prof. Alexandro Castellanos for his help in getting us started with the National Instruments myRIO/sbRIO boards.

Disclosures. ABP: SPKL LLC (I, P)

Data availability. Data underlying the results presented in this paper are not publicly available at this time but may be obtained from the authors upon reasonable request.

Biomedical Optics EXPRESS

References

1. D. A. Boas and A. G. Yodh, "Spatially varying dynamical properties of turbid media probed with diffusing temporal light correlation," J. Opt. Soc. Am. A **14**(1), 192–215 (1997).
2. T. Durduran and A. G. Yodh, "Diffuse correlation spectroscopy for non-invasive, micro-vascular cerebral blood flow measurement," NeuroImage **85**, 51–63 (2014).
3. E. M. Buckley, A. B. Parthasarathy, P. E. Grant, *et al.*, "Diffuse correlation spectroscopy for measurement of cerebral blood flow: future prospects," Neurophotonics **1**(1), 011009 (2014).
4. E. M. Buckley, N. M. Cook, T. Durduran, *et al.*, "Cerebral hemodynamics in preterm infants during positional intervention measured with diffuse correlation spectroscopy and transcranial doppler ultrasound," Opt. Express **17**(15), 12571–12581 (2009).
5. D. R. Busch, W. B. Baker, C. D. Mavroudis, *et al.*, "Noninvasive optical measurement of microvascular cerebral hemodynamics and autoregulation in the neonatal ecmo patient," Pediatr. Res. **88**(6), 925–933 (2020).
6. T. Durduran, C. Zhou, B. L. Edlow, *et al.*, "Transcranial optical monitoring of cerebrovascular hemodynamics in acute stroke patients," Opt. Express **17**(5), 3884–3902 (2009).
7. G. Yu, T. Durduran, G. Lech, *et al.*, "Time-dependent blood flow and oxygenation in human skeletal muscles measured with noninvasive near-infrared diffuse optical spectroscopies," J. Biomed. Opt. **10**(2), 024027 (2005).
8. G. Yu, T. F. Floyd, T. Durduran, *et al.*, "Validation of diffuse correlation spectroscopy for muscle blood flow with concurrent arterial spin labeled perfusion mri," Opt. Express **15**(3), 1064–1075 (2007).
9. A. S. Kogler, T. V. Bilfinger, R. Galler, *et al.*, "Fiber-optic monitoring of spinal cord hemodynamics in experimental aortic occlusion," Anesthesiology **123**(6), 1362–1373 (2015).
10. G. Yu, "Diffuse correlation spectroscopy (dcs): A diagnostic tool for assessing tissue blood flow in vascular-related diseases and therapies," Current Medical Imaging Reviews **8**(3), 194–210 (2012).
11. T. Durduran, R. Choe, W. B. Baker, *et al.*, "Diffuse optics for tissue monitoring and tomography," Rep. Prog. Phys. **73**(7), 076701 (2010).
12. D. Wang, A. B. Parthasarathy, W. B. Baker, *et al.*, "Fast blood flow monitoring in deep tissues with real-time software correlators," Biomed. Opt. Express **7**(3), 776–797 (2016).
13. J. Dong, R. Bi, J.-H. Ho, *et al.*, "Diffuse correlation spectroscopy with a fast Fourier transform-based software autocorrelator," J. Biomed. Opt. **17**(9), 097004 (2012).
14. M. Tivnan, R. Gurjar, D. E. Wolf, *et al.*, "High frequency sampling of ttl pulses on a raspberry pi for diffuse correlation spectroscopy applications," Sensors **15**(8), 19709–19722 (2015).
15. D. Magatti and F. Ferri, "Fast multi-tau real-time software correlator for dynamic light scattering," Appl. Opt. **40**(24), 4011–4021 (2001).
16. Q. Wang, M. Pan, L. Kreiss, *et al.*, "A comprehensive overview of diffuse correlation spectroscopy: Theoretical framework, recent advances in hardware, analysis, and applications," NeuroImage **298**, 120793 (2024).
17. S. A. Carp, M. B. Robinson, and M. A. Franceschini, "Diffuse correlation spectroscopy: current status and future outlook," Neurophotonics **10**(01), 013509 (2023).
18. G. Dietsche, M. Ninck, C. Ortolf, *et al.*, "Fiber-based multispeckle detection for time-resolved diffusing-wave spectroscopy: characterization and application to blood flow detection in deep tissue," Appl. Opt. **46**(35), 8506–8514 (2007).
19. W. Liu, R. Qian, S. Xu, *et al.*, "Fast and sensitive diffuse correlation spectroscopy with highly parallelized single photon detection," APL Photonics **6**(2), 026106 (2021).
20. E. J. Sie, H. Chen, E.-F. Saung, *et al.*, "High-sensitivity multispeckle diffuse correlation spectroscopy," Neurophotonics **7**(03), 035010 (2020).
21. M. B. Robinson, D. A. Boas, S. Sakadžic, *et al.*, "Interferometric diffuse correlation spectroscopy improves measurements at long source–detector separation and low photon count rate," J. Biomed. Opt. **25**(09), 097004 (2020).
22. W. Zhou, O. Kholiqov, J. Zhu, *et al.*, "Functional interferometric diffusing wave spectroscopy of the human brain," Sci. Adv. **7**(20), eabe0150 (2021).
23. E. James and S. Powell, "Fourier domain diffuse correlation spectroscopy with heterodyne holographic detection," Biomed. Opt. Express **11**(11), 6755–6779 (2020).
24. C. P. Valdes, H. M. Varma, A. K. Kristoffersen, *et al.*, "Speckle contrast optical spectroscopy, a non-invasive, diffuse optical method for measuring microvascular blood flow in tissue," Biomed. Opt. Express **5**(8), 2769–2784 (2014).
25. J. Xu, A. K. Jahromi, J. Brake, *et al.*, "Interferometric speckle visibility spectroscopy (isvs) for human cerebral blood flow monitoring," APL Photonics **5**(12), 126102 (2020).
26. W. Zhou, M. Zhao, O. Kholiqov, *et al.*, "Multi-exposure interferometric diffusing wave spectroscopy," Opt. Lett. **46**(18), 4498–4501 (2021).
27. J. Sutin, B. Zimmerman, D. Tyulmankov, *et al.*, "Time-domain diffuse correlation spectroscopy," Optica **3**(9), 1006–1013 (2016).
28. D. Borycki, O. Kholiqov, S. P. Chong, *et al.*, "Interferometric near-infrared spectroscopy (inirs) for determination of optical and dynamical properties of turbid media," Opt. Express **24**(1), 329–354 (2016).
29. A. M. Safi, S. Moka, M. Harrah, *et al.*, "Quantitative measurement of static and dynamic tissue optical properties with continuous wave pathlength resolved diffuse correlation spectroscopy," in *Biophotonics Congress 2021* (Optica Publishing Group, 2021), p. BTh1B.6.

Biomedical Optics EXPRESS

30. A. Tsalach, Y. Metzger, I. Breskin, *et al.*, "Ultrasound modulated light blood flow measurement using intensity autocorrelation function: a Monte-Carlo simulation," in *Photons Plus Ultrasound: Imaging and Sensing 2014*, vol. 8943, A. A. Oraevsky and L. V. Wang, eds., International Society for Optics and Photonics (SPIE, 2014), p. 89433N.
31. M. B. Robinson, S. A. Carp, A. Peruch, *et al.*, "Characterization of continuous wave ultrasound for acousto-optic modulated diffuse correlation spectroscopy (aom-dcs)," Biomed. Opt. Express **11**(6), 3071–3090 (2020).
32. S. A. Carp, D. Tamborini, D. Mazumder, *et al.*, "Diffuse correlation spectroscopy measurements of blood flow using 1064 nm light," J. Biomed. Opt. **25**(09), 097003 (2020).
33. N. Ozana, A. I. Zavriyev, D. Mazumder, *et al.*, "Superconducting nanowire single-photon sensing of cerebral blood flow," Neurophotonics **8**(03), 035006 (2021).
34. N. Ozana, N. Lue, M. Renna, *et al.*, "Functional time domain diffuse correlation spectroscopy," Front. Neurosci. **16**, 932119 (2022).
35. J. D. Johansson, D. Portaluppi, M. Buttafava, *et al.*, "A multipixel diffuse correlation spectroscopy system based on a single photon avalanche diode array," J. Biophotonics **12**(11), e201900091 (2019).
36. F. M. Della Rocca, E. J. Sie, R. Catoen, *et al.*, "Field programmable gate array compression for large array multispeckle diffuse correlation spectroscopy," J. Biomed. Opt. **28**(05), 057001 (2023).
37. M. A. Wayne, E. J. Sie, A. C. Ulku, *et al.*, "Massively parallel, real-time multispeckle diffuse correlation spectroscopy using a 500×500 spad camera," Biomed. Opt. Express **14**(2), 703–713 (2023).
38. F. M. Della Rocca, E. J. Sie, A. T. Erdogan, *et al.*, "A 512×512 spad laser speckle autocorrelation imager in stacked 65/40nm cmos," in *2024 IEEE Symposium on VLSI Technology and Circuits (VLSI Technology and Circuits)*, (2024), pp. 1–2.
39. W. Lin, D. R. Busch, C. C. Goh, *et al.*, "Diffuse correlation spectroscopy analysis implemented on a field programmable gate array," IEEE Access **7**, 122503–122512 (2019).
40. C. H. Moore and W. Lin, "Fpga correlator for applications in embedded smart devices," Biosensors **12**(4), 236 (2022).
41. A. Biswas and A. B. Parthasarathy, "Lossless compressed sensing of photon counts for fast diffuse correlation spectroscopy," IEEE Access **10**, 129754–129762 (2022).
42. M. Mokin, S. Thanki, P. P. S. Mohammad, *et al.*, "Preliminary experience with diffuse correlation spectroscopy in acute ischemic stroke neurointerventional procedures," J. NeuroIntervent Surg. **16**(6), 624–631 (2024).
43. A. Biswas, S. Moka, A. Muller, *et al.*, "Fast diffuse correlation spectroscopy with a low-cost, fiber-less embedded diode laser," Biomed. Opt. Express **12**(11), 6686–6700 (2021).
44. J. W. Goodman, *Speckle Phenomena in Optics: Theory and Applications*, 2nd ed. (SPIE Press, 2020), chap. 8.
45. K. Schätzel, "Noise on photon correlation data. i. autocorrelation functions," Quantum Opt. **2**(4), 287–305 (1990).
46. C. Zhou, G. Yu, D. Furuya, *et al.*, "Diffuse optical correlation tomography of cerebral blood flow during cortical spreading depression in rat brain," Opt. Express **14**(3), 1125–1144 (2006).
47. Y. Wang, Y. Liu, A. Gorman, *et al.*, "A computationally efficient approach for diffuse correlation spectroscopy implemented on a field programmable gate array," in *2025 IEEE Biomedical Circuits and Systems Conference (BioCAS)*, (2025), pp. 116–120.
48. Y. Wang, Y. Liu, A. Gorman, *et al.*, "Characterization of a pixel-level binarized autocorrelator for large array multispeckle diffuse correlation spectroscopy under photon-starved conditions," IEEE Transactions on Biomedical Circuits and Systems pp. 1–12 (2026).
49. H. Zhao, E. Sathialingam, K. R. Cowdrick, *et al.*, "Comparison of diffuse correlation spectroscopy analytical models for measuring cerebral blood flow in adults," J. Biomed. Opt. **28**(12), 126005 (2023).
50. H. Zhao, E. Sathialingam, and E. M. Buckley, "Accuracy of diffuse correlation spectroscopy measurements of cerebral blood flow when using a three-layer analytical model," Biomed. Opt. Express **12**(11), 7149–7161 (2021).
51. S. A. Carp, P. Farzam, N. Redes, *et al.*, "Combined multi-distance frequency domain and diffuse correlation spectroscopy system with simultaneous data acquisition and real-time analysis," Biomed. Opt. Express **8**(9), 3993–4006 (2017).
52. D. Tamborini, P. Farzam, B. B. Zimmermann, *et al.*, "Development and characterization of a multidistance and multiwavelength diffuse correlation spectroscopy system," Neurophotonics **5**(1), 011015 (2017).
53. M. B. Robinson, M. Renna, N. Otic, *et al.*, "Pathlength-selective, interferometric diffuse correlation spectroscopy," IEEE J. Sel. Top. Quantum Electron. **31**(4), 7400814 (2025).
54. M. Zhao, W. Zhou, S. Aparanji, *et al.*, "Interferometric diffusing wave spectroscopy imaging with an electronically variable time-of-flight filter," Optica **10**(1), 42–52 (2023).
55. W. Zhou, O. Kholiqov, S. P. Chong, *et al.*, "Highly parallel, interferometric diffusing wave spectroscopy for monitoring cerebral blood flow dynamics," Optica **5**(5), 518–527 (2018).